Hot spots in energetic materials generated by infrared and ultrasound, detected by thermal imaging microscopy

Ming-Wei Chen, Sizhu You, Kenneth S. Suslick, and Dana D. Dlott

Citation: Review of Scientific Instruments **85**, 023705 (2014); doi: 10.1063/1.4864197
View online: http://dx.doi.org/10.1063/1.4864197
View Table of Contents: http://scitation.aip.org/content/aip/journal/rsi/85/2?ver=pdfcov
Published by the AIP Publishing

Hot spots in energetic materials generated by infrared and ultrasound, detected by thermal imaging microscopy

Ming-Wei Chen, Sizhu You, Kenneth S. Suslick, and Dana D. Dlott[a)]
School of Chemical Sciences and Fredrick Seitz Materials Research Laboratory, University of Illinois at Urbana-Champaign, Urbana, Illinois 61801, USA

(Received 10 December 2013; accepted 22 January 2014; published online 12 February 2014)

We have observed and characterized hot spot formation and hot-spot ignition of energetic materials (EM), where hot spots were created by ultrasonic or long-wavelength infrared (LWIR) exposure, and were detected by high-speed thermal microscopy. The microscope had 15–20 μm spatial resolution and 8.3 ms temporal resolution. LWIR was generated by a CO_2 laser (tunable near 10.6 μm or 28.3 THz) and ultrasound by a 20 kHz acoustic horn. Both methods of energy input created spatially homogeneous energy fields, allowing hot spots to develop spontaneously due to the microstructure of the sample materials. We observed formation of hot spots which grew and caused the EM to ignite. The EM studied here consisted of composite solids with 1,3,5-trinitroperhydro-1,3,5-triazine crystals and polymer binders. EM simulants based on sucrose crystals in binders were also examined. The mechanisms of hot spot generation were different with LWIR and ultrasound. With LWIR, hot spots were most efficiently generated within the EM crystals at LWIR wavelengths having longer absorption depths of ~25 μm, suggesting that hot spot generation mechanisms involved localized absorbing defects within the crystals, LWIR focusing in the crystals or LWIR interference in the crystals. With ultrasound, hot spots were primarily generated in regions of the polymer binder immediately adjacent to crystal surfaces, rather than inside the EM crystals. © *2014 AIP Publishing LLC*. [http://dx.doi.org/10.1063/1.4864197]

I. INTRODUCTION

The initiation of energetic materials (EM) is usually associated with the creation of "hot spots," which are small regions (typically μm to mm) where the energy input to initiate the material has been temporarily concentrated.[1–3] When a hot spot ignites, it might simply die out or it might undergo explosive growth leading to widespread EM ignition. Hot spot formation depends on the EM microstructure and the method of energy input. Most of the properties of hot spots have only been inferred from observations after their formation, and despite the importance of hot spots to EM ignition, there have been few direct, real-time imaging measurements.[2] In this article, we describe a mid-wavelength infrared (MWIR) microscopy apparatus for real-time observations of hot spots in EM and EM simulants. The EM used here was a well-known high-performance molecular explosive, RDX (1,3,5-trinitroperhydro-1,3,5-triazine). We used our MWIR microscope to detect hot spots created in two ways, using either THz radiation from a long-wavelength IR (LWIR) laser or an ultrasonic horn. These methods do not create hot spots by inputting energy into a tiny spot,[4] or by spiking the EM with tiny absorbing inclusions,[5] but instead they input energy in a spatially diffuse, homogeneous manner, which allowed the hot spots to develop spontaneously in microstructured sample materials.

Hot spot temperatures needed to initiate RDX depend on many factors, including the sample geometry and microstructure, the method of energy input, and the hot spot sizes and lifetimes.[6,7] As a benchmark, it has been shown by calorimetry that RDX decomposes with a strong exotherm when heated to 530 K.[8]

Almost all previous observations of hot spots in EM relied on visible emission techniques such as high-speed photography.[1,2,9–12] Notable exceptions were two 1992 studies by Woody,[13,14] who used a fast IR detector array to obtain single time-gated images of shear bands created in salt crystals subjected to low-velocity impacts, and more recent works by Dickson and co-workers[15] and Perry and co-workers,[16] who studied impacted EM with a combination of visible and IR imaging.

The energy needed to initiate an EM may be input in many ways, ranging from gentle (e.g., a spark) to severe (e.g., a km s^{-1} impact). All these methods have one thing in common: the energy that initiates the EM is generally quite a bit less than what is needed to raise the bulk EM temperature to the ignition point. For instance, in low-velocity initiation (e.g., when a weight is dropped a few tens of cm onto an EM causing it to explode), the kinetic energy of the dropping weight is usually not enough to heat the bulk EM by even 10 K.[3,17] Such observations clearly imply that hot-spot forming energy concentration mechanisms must be at work in EM initiation.[9] There have been many mechanisms proposed for the origin of hot spots. Void collapse, friction between sliding surfaces, localized adiabatic shear, or heating at crack tips or dislocation pile ups, among other possibilities, have been proposed as hot-spot creators, under conditions of low-velocity impact.[1] Most practical EM have complex microstructural features. For instance, a plastic-bonded explosive (PBX) generally

a)Author to whom correspondence should be addressed. Electronic mail: dlott@illinois.edu

consists of explosive crystals having a bimodal size distribution, of "fine" particles in the 1–50 μm range and "coarse" particles in the 0.1–1 mm range, along with a few percent of polymer binder.[18] Such composites have microstructural features including polymer-particle interfaces, cracks and voids within the coarse particles, and also sharp contact points between crystalline particles. All such structural features are, at least in theory, sources of potential hot spot.

We must differentiate here between the hot spots formed in solid composites in the present study from those created in liquids during ultrasonic irradiation. Acoustic cavitation (the formation, growth, and implosive collapse of bubbles in a liquid) creates a very different hot spot in liquids exposed to high-intensity ultrasound. The heating mechanism is adiabatic compression of the gas inside bubbles.[19,20] The transient conditions formed during acoustic cavitation can give rise to local effective temperatures greater than 20 000 K, pressures of ~1 kbar, and substantial ionization of an optically opaque plasma, all on a nanosecond time frame. These extreme conditions decay with immense cooling rates $>10^{12}$ K s^{-1}.[21–23] In solids, such as those studied here, the mechanisms that give rise to acoustic cavitation are not available and hot spots in solids are therefore rather different in origin and intensity.

The instrument described here was based on a MWIR camera and a MWIR microscope objective that provided MWIR resolution comparable to the camera's 15 μm pixel pitch. The camera acquired frames at up to 120 Hz, and each frame may be captured with an integration time ranging from 0.48 μs to 20 ms. The camera could produce movies of hot spot dynamics with an interframe interval of 8.3 ms, which was sufficient to characterize the LWIR and ultrasound hot-spot generation processes studied here.

In the rest of this paper, we describe and characterize the IR microscopy setup, the LWIR and ultrasound sources, and the EM samples used. Then we present results obtained on LWIR and ultrasound-irradiated RDX samples showing the development of hot spots that initiated rapid thermal decomposition of the sample materials.

II. EXPERIMENTAL

The experimental apparatus, consisting of a thermal imaging microscope (IR camera and microscope objective) and either LWIR laser or ultrasonic horn, is diagrammed in Figs. 1(a) and 1(b).

A. Thermal imaging microscope

The thermal imaging camera (IRE-640M, Sofradir-EC, Inc., Fairfield, NJ) had 640 × 512 cooled HgCdTe pixels with a 15 μm pitch, with sensitivity in the 3.7–4.8 μm range. It had an integrated cooler assembly that could reach as low as 90 K. The cold shield around the detector array had a numerical aperture of N.A. = 0.25, so the theoretical spatial resolution in the MWIR was on the order of R ≈ 0.61λ/N.A. ≈ 10 μm. This resolution estimate, assuming an objective lens whose N.A. was similar to the cold shield, suggests the MWIR spatial resolution could be limited by the 15 μm pixel size. The IR objective (Asio 1×, Janos Tech, Keene, NH) had a magnification of 1× and N.A. = 0.22. The working distance was 60 mm. The field-of-view, based on the size of the 640 × 512 image array and the objective magnification, was 9.6 × 7.68 mm^2.

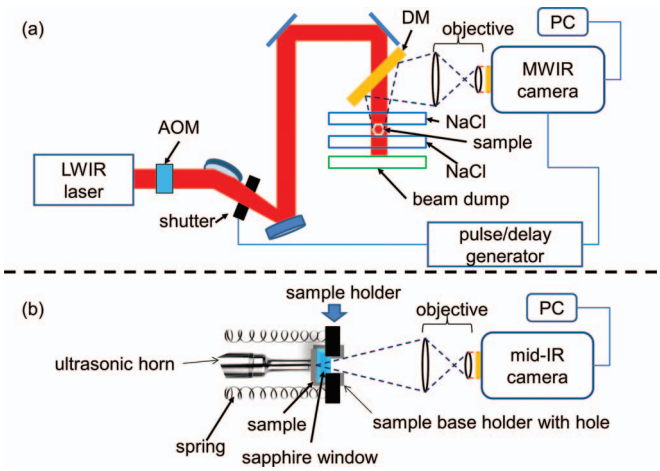

FIG. 1. (a) Schematic of thermal imaging microscope used to study hot spots created by long-wavelength infrared (LWIR) laser beams. Key: MWIR = mid-wavelength IR, DM = dichroic mirror, AOM = acousto-optic modulator. (b) Schematic for MWIR microscope to study hot spots created by ultrasound.

B. LWIR laser

The apparatus for irradiating samples with THz radiation from a LWIR laser and observing them with MWIR microscopy is depicted in Fig. 1(a). The continuous-wave, grating-tunable RF waveguide CO_2 laser (LC-50, DeMaria ElectroOptics System, Inc.) could produce ~50 W on discrete emission lines. The relevant portion of the tuning curve of the CO_2 laser is shown in Fig. 2(a). An acousto-optic

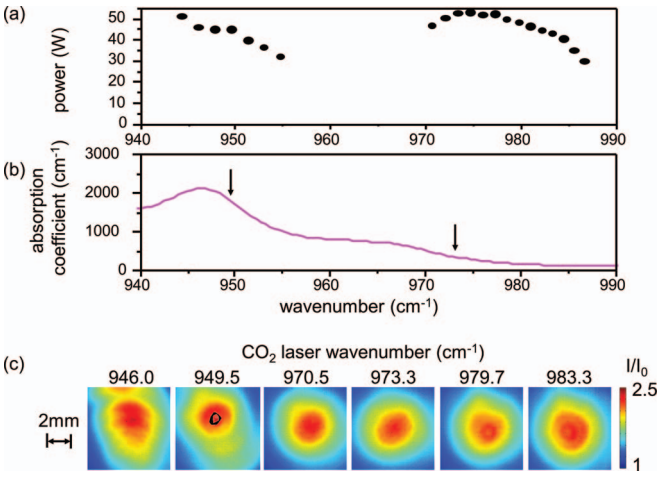

FIG. 2. (a) Output powers of line-tunable CO_2 long-wavelength infrared (LWIR) laser. (b) Infrared spectrum of RDX powder in a KBr pellet. The arrows denote LWIR wavenumbers used in thermal imaging measurements. (c) Images of LWIR laser beam profiles at the indicated LWIR wavenumbers. The laser power was adjusted at each wavenumber to produce the same maximum thermal emission intensity from a glass slide. In the 949.5 cm^{-1} panel, an image of a typical RDX crystal was superimposed to show that the crystals were exposed to spatially uniform LWIR irradiation.

modulator (AOM) (AGM-406B1 with GE4030 driver, IntraAction Corp.) was used to gate and adjust the intensity of the first-order diffraction beam, which was sent to the sample. The small amount of leakage light collinear with the diffracted beam was eliminated using an electronic shutter (LSTXY-W8, nmLaser Products, Inc.). The LWIR beam, which had a near-Gaussian spatial profile, was focused with a ZnSe lens to an approximate diameter ($1/e^2$ intensity points) of 2–3 mm. Because the sample materials were optically thick in the MWIR region, the laser-irradiated materials were observed in reflection mode, so that the MWIR microscope observed the side of the sample materials that was irradiated by the LWIR beam. The MWIR image was isolated from the LWIR laser beam, as depicted in Fig. 1(a), using a dichroic mirror (II-VI Corp.) that transmitted LWIR and reflected MWIR.

C. Ultrasound source

As depicted in Fig. 1(b), the ultrasound source was a 20 kHz ultrasonic horn (CV33, Sonics and Materials, Inc.), with tip diameter ~13 mm. The Ti alloy tip was polished flat before each use to create a spatially uniform acoustic field. The output amplitude of the horn was adjusted by a controller (Vibracell VCX-750, Sonics and Materials, Inc.) in the region between 20% and 100% of the peak amplitude of 114 μm.

The samples for ultrasound measurements were disks consisting of RDX crystals embedded in polymer binder, described below. The disks were pressed between the Ti horn and a 25.4 mm diameter MWIR sapphire window. The sample and window were mounted in a stainless-steel holder having a 13 mm diameter aperture for the thermal imaging microscope. The horn was mounted to the sample holder using four spring-loaded 3 mm diameter guide rods. The pressure between the horn and sample was adjusted using springs of different stiffness. After some trial and error, we settled on a pressure of 10^6 N m^{-2}, which produced a good acoustic contact but which did not noticeably deform the embedded RDX crystals.

D. Sample preparation

The LWIR experiments looked at individual RDX crystals, or a disk of RDX-based PBX. The crystals were grown from RDX furnished by Dr. Dan Hooks of Los Alamos National Laboratory, recrystallized once to assure purity and dissolved in acetone to produce nearly saturated solutions. These solutions were transferred to small beakers loosely covered with watch glasses to create slow evaporation over several days. The beakers were immersed to the solution level in a temperature-controlled sandbox at 30 °C. Selected crystals in the 300–750 μm size range were immobilized by sandwiching them between two salt (NaCl) windows. The PBX was furnished by Professor Nick Glumac of the University of Illinois, who obtained it from Teledyne Risi, Inc. (Tracy, CA). This material, denoted PBX 9407, consisted of 94% RDX and 6% FPC-461 polymer binder. This binder material was a vinyl chloride: chlorotrifluoroethylene copolymer. Estane is a polyurethane copolymer used as a binder material in some PBX, for instance, PBX 9501.[18] The estane polymer films used here[24] (Estane 5703, Lubrizon, Inc.) were produced by dissolving estane in methylethylketone and evaporating the solution onto salt windows.

The ultrasound experiments looked at two kinds of samples having crystals embedded in a polymer binder. The acoustic horn contacted only the binder and did not touch the crystals. RDX was embedded in polydimethylsiloxane (PDMS) (Dow Corning Sylgard 182), which is a binder that has also been used for PBX. First, a thin 300 μm layer of PDMS was coated onto a sapphire window and allowed to cure. Then a second PDMS layer ~500 μm thick was added, and RDX crystals were stuck into the semi-liquid PDMS before curing. After the PDMS with embedded RDX crystals was cured, a final ~500 μm thick PDMS layer was coated over the crystals so the crystal were fully embedded in PDMS. A similar procedure was used to make an energetic simulant material where the crystals were sucrose (250–500 μm) and the binder was hydroxy-terminated polybutadiene (HTPB) cured with 12% methylene diphenyl diisocyanate (PAPI 94 from Dow Chemical). Sucrose is known to be a good simulant because it has a reasonable mechanical and acoustic match to dense, brittle EM crystals.[25]

III. RESULTS

A. RDX LWIR absorption

A KBr pellet was made with a known density of RDX, and its LWIR spectrum was measured using a Fourier-transform IR spectrometer. We then computed the absorption coefficients α in the vicinity of 10 μm for this pellet, and multiplied these absorption coefficients by the ratio of the density of pure crystalline RDX to the RDX density in the pellet. Note these absorption coefficients refer to randomly oriented powder at the single-crystal density in unpolarized light, whereas the thermal imaging experiments were performed with individual crystals in polarized light. A portion of the RDX pellet IR spectrum is shown in Fig. 2(b). Keeping in mind that the RDX chemical formula can be written as $(CH_2–N–NO_2)_3$, the observed transitions in this region involved an admixture of CH_2 bending and $N–NO_2$ stretching.[26] Comparing the RDX spectrum to the CO_2 laser tuning curve in Fig. 2(a), we decided to conduct thermal imaging measurements at two LWIR wavenumbers where the RDX absorption was stronger or weaker, i.e., 949.5 cm^{-1} and 973.3 cm^{-1}, respectively (indicated by the arrows in Fig. 2(b)), where the absorption coefficients were $\alpha = 2000$ cm^{-1} and $\alpha = 400$ cm^{-1}, respectively. This corresponds to $1/e$ absorption depths at 949.5 cm^{-1} of 5 μm, and at 973.3 cm^{-1} the absorption depth was 25 μm.

B. LWIR laser beam

The profiles of the CO_2 laser beams, which were roughly 2–3 mm in diameter, were characterized by imaging a glass window irradiated by the laser beam. Glass was chosen because the LWIR absorption coefficient was roughly wavelength-independent in the relevant spectral region, and

image distortion by thermal conductivity would be minimal. For radial thermal conduction, which is one-dimensional thermal conduction in a half-space, the thermal diffusion length $d(t)$ is a function of time given by[27]

$$d(t) = (1/2)(2Dt)^{1/2}. \quad (1)$$

The thermal diffusivity of window glass $D = 3.4 \times 10^{-3}$ $cm^2\ s^{-1}$, so during a 450 ms laser pulse, the thermal diffusion length would be $d = 200$ μm. That amount of thermal diffusion would minimally distort images of 2–3 mm diameter beams.

At each LWIR wavelength, a laser profile image using 100 μs integration time was obtained after irradiating the glass for 450 ms, as shown in Fig. 2(c). As seen in Fig. 2(c), the beam shape varied undesirably as we tuned through different laser lines. In order to compensate for those variations, we adjusted the AOM drive power so that the glass temperature in the uniform part of the beam center was the same at each LWIR wavenumber. In the image taken at 949.5 cm^{-1}, we superimposed the image of one RDX crystal to show that a typically sized (300–750 μm) RDX crystal at the beam center was irradiated nearly uniformly by the CO_2 LWIR laser beam.

C. Spatial resolution of the MWIR microscope

To determine the spatial resolution of the IR microscope, we obtained images of a calibrated reticle having 10 μm, 50 μm, and 100 μm line spacings. A visible image (in transmission) of this reticle is shown in Fig. 3(a), along with the corresponding MWIR image in Fig. 3(b). Note the visible image shows dark lines against a clear glass slide, whereas the MWIR emission image shows brighter, more emissive lines against a dark background. The 10 μm lines could not be resolved in the IR, but the 50 μm lines were well-resolved. Figure 3(c) is a line scan of the MWIR image of the reticle along the horizontal line indicated in Fig. 3(b). Figures 3(b) and 3(c) indicate that the MWIR emission from each narrow line of the reticle was concentrated in single 15 μm pixels, and the intensity in adjacent pixels was a factor of five or more less than in the main pixel. Thus, the spatial resolution of the MWIR microscope images was on the order of 15–20 μm.

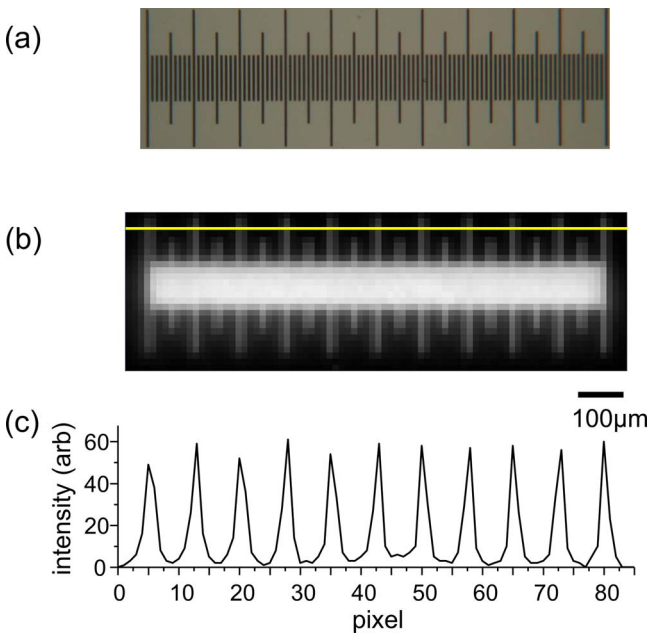

FIG. 3. (a) Optical image, obtained in transmission, of a calibrated reticle having lines with spacings 10 μm, 50 μm, and 100 μm on a glass slide. (b) MWIR emission image of the same reticle. (c) Intensity scan along the horizontal line in (b). The spacing between pixels was 15 μm.

D. Temperature and emissivity image calibration

RDX and the polymers used here are molecular materials and dielectrics, so the MWIR emissivities $\varepsilon(\nu,T)$ have complicated dependences on IR frequencyν and temperature, which are related to the structured "fingerprint" MWIR absorptions. The emissivities also depend on the material thickness in regions where these materials are optically thin in the MWIR.

After the MWIR camera was calibrated and corrected for nonuniform pixel sensitivity[28] using protocols provided by the manufacturer, we obtained images of RDX up to 400 K, safely below the onset of RDX thermal decomposition, and estane up to 410 K, just before the polymer began to darken. Figures 4(a) and 4(b) are room-temperature (298 K) images of a few RDX crystals adjacent to an estane slab, using 1.1 ms and 0.1 ms integration times, respectively. The sample materials were placed on IR-transparent salt windows backed by a gold mirror with exceptionally low IR emissivity, to create a black background. An image of the same sample at 373 K with 0.1 ms integration time is shown in Fig. 4(c), and the computed image I/I_0 = [intensity (373 K)]/[intensity (298 K)], is shown in Fig. 4(d). Note how this ratio decreases at the right edge of the estane film, where the film is thinner.

The intensity ratio I/I_0 can be expressed as[28]

$$\frac{I(T_2)}{I_0(T_1)} = \frac{\int_{\lambda_1}^{\lambda_2} \varepsilon(\lambda, T_2) I(\lambda, T_2) d\lambda}{\int_{\lambda_1}^{\lambda_2} \varepsilon(\lambda, T_1) I(\lambda, T_1) d\lambda}, \quad (2)$$

where $I(\lambda,T)$ is the blackbody spectral irradiance, and the limits of integration for our camera were $\lambda_1 = 3.7$ μm and $\lambda_2 = 4.8$ μm. Figure 4(e) is a plot of measured values of I/I_0 for RDX and estane versus T_2 for $T_1 = 298$ K. Also in Fig. 4(e) is the computed result for a blackbody with $\varepsilon(\lambda,T) = 1$. The smooth curves through the RDX and estane data in Fig. 4(e) were phenomenological fitting functions of the form,

$$T(K) = a\left(\frac{I}{I_0}\right)^b. \quad (3)$$

In our displayed results, we computed temperatures using an effective emissivity for every pixel of each image. We can also compute overall emissivities for RDX and estane, based on data from the brightest regions in Fig. 4(e), where these materials were presumably approaching the optically thick limit. These effective emissivities are shown in Fig. 4(f). The dashed part of the RDX emissivity curve is an analytical continuation to higher temperatures of the measured data, based on Eq. (3).

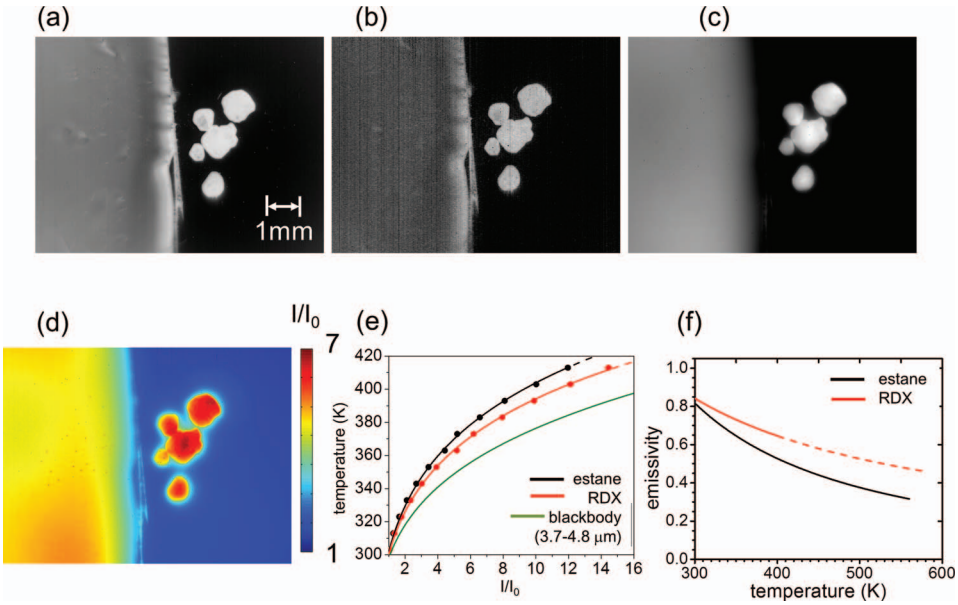

FIG. 4. (a) Ambient temperature (298 K) MWIR image of an estane slab (left) and a few RDX crystals (right), with 1.1 ms integration. (b) Image of the same sample with 0.1 ms integration. (c) Image of the same sample at 373 K with 0.1 ms integration. (d) Computed image of the ratio I/I_0 = [intensity (373 K)]/[intensity (298 K)]. (e) Measured values of I/I_0 for RDX and estane. The smooth curves were fitted to the data using Eq. (3). (f) Emissivities of RDX and estane in the 3.7–4.8 MWIR range. The dashed part of the RDX curve is an analytical continuation based on fitting the data in (3).

E. LWIR flash-heating of RDX

Figure 5 shows results of four experiments where RDX crystals were exposed to the LWIR laser beam. In Fig. 5(a), the LWIR laser was tuned to the less strongly absorbed LWIR wavenumber 973 cm^{-1}, and in Fig. 5(b) the laser was tuned to the more strongly absorbed LWIR wavenumber 949.5 cm^{-1}.

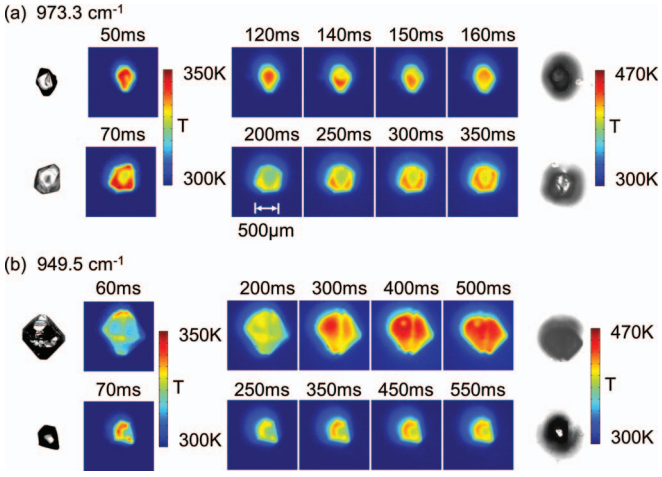

FIG. 5. Thermal images from individual RDX crystals irradiated by a LWIR laser beam. The images of the RDX crystals at far left and far right were obtained with an optical microscope before and after LWIR irradiation. The high temperatures >470 K at longer times, as seen in the post-heating visible images at the far right indicate that the crystals were exothermically decomposed by LWIR. (a) The LWIR wavenumber was 973.3 cm^{-1} (which was less-strongly absorbed) and (b) 949.5 cm^{-1} (more-strongly absorbed). The initially formed hot spots, which are best seen at shorter times (50–70 ms), were more prominent with the less-strongly absorbed 973.3 cm^{-1} LWIR (see RDX absorption spectrum in Fig. 2(b)). The latter thermal micrographs (at 250–550 ms) indicate the highly exothermic processes created by RDX ignition.

The LWIR laser beam intensity was adjusted so the RDX would undergo thermal decomposition on a time scale that was convenient for the maximum 8.3 ms interframe rate of the MWIR camera. The CO_2 laser was 18 W and the RDX crystals decomposed within a few hundred milliseconds. The MWIR images in Fig. 5 were obtained with 100 μs integration times. Over the course of a typical experiment (~500 ms), we obtained about 60 images, and we selected a few representative images to display in Fig. 5.

In Fig. 5, we also display images of the four RDX crystals before and after flash-heating, obtained using an optical microscope. The optical microscope shows fine details better than the lower-resolution MWIR microscope. The optical images were digitally scaled using calibrated reticles, to be the same size as the MWIR images, and the optical images were rotated to coincide with the MWIR images. Comparing the optical images before and after heating show that RDX was decomposed by the LWIR laser beam.

Figure 5 has three quite striking features: (1) prominent hot spots were created by the LWIR laser prior to thermal decomposition, despite the near-uniformity of the LWIR beam, (2) the LWIR-heated RDX crystals at some brief times during the image sequences reached the ~500 K temperature associated with highly exothermic decomposition processes, and (3) hot spots in the RDX crystals were more prominent in Fig. 5(a) than in Fig. 5(b), and Fig. 5(a) was where the LWIR was more weakly absorbed.

The hot spots are best seen in Fig. 5 during the earlier stages of laser heating (e.g., 50–70 ms). After those times the hot spots have grown, causing ignition of entire crystals. RDX ignition was confirmed by the brief appearances of widespread temperatures >470 K, and by the optical images of the crystals after irradiation. With the more weakly absorbed 973.3 cm^{-1} LWIR, the initial hot spots (formed

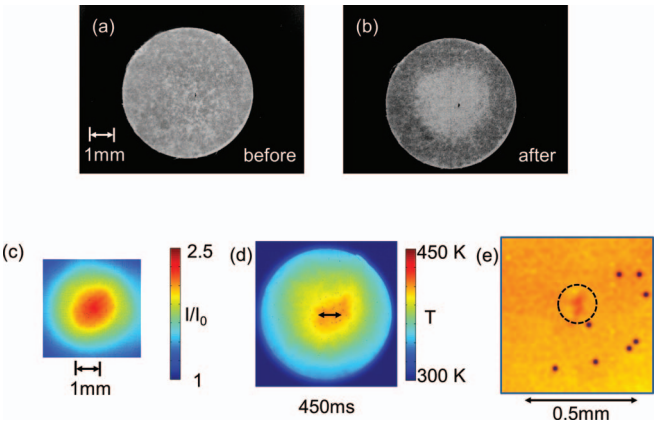

FIG. 6. IR images of a plastic-bonded explosive, PBX 9407, consisting of RDX crystals and a vinyl chloride copolymer binder before (a) and after (b) irradiation with LWIR (973.3 cm^{-1}). (c) Image of the LWIR beam on a glass flat showing the uniformity of the central portion of the near-Gaussian profile beam. (d) Thermal image of LWIR-irradiated PBX at a time delay of 450 ms, showing a temperature profile indicative of nonuniform heating and hot spot formation. (e) Expanded view of the center of the LWIR-heated PBX at 450 ms. The tiny dark spots are artifacts from bad pixels. A prominent hot spot is highlighted by the dashed circle.

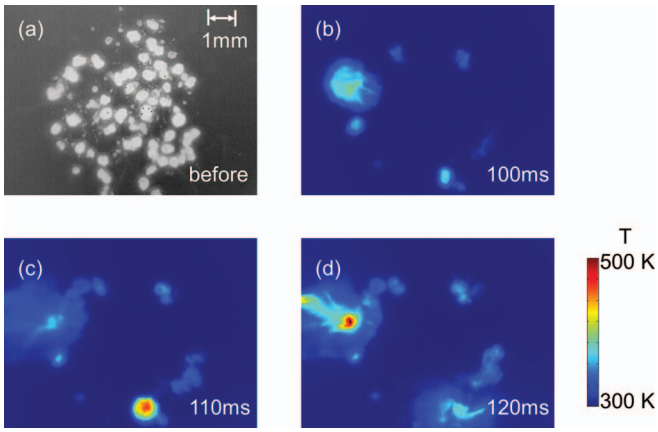

FIG. 7. (a) IR image of a sample consisting of RDX crystals (brighter regions) embedded in (darker) PDMS polymer. (b)–(d) False temperature images of the sample during ultrasound irradiation showing hot spots produced in a few of the RDX crystals.

early at 50–70 ms) were more prominent and hotter than with the more strongly absorbed 949.5 cm^{-1} LWIR, although once the crystals have ignited the ignition temperatures were about the same with both LWIR wavenumbers. The hot spots appear to be associated with topographic features of the individual RDX crystals such as tilted crystal planes and edges, as judged by comparing the optical "before" images with the MWIR images. The more efficient generation of hot spots using the more weakly absorbing LWIR was an effect that we have seen in more than ten crystals (four of which are shown in Fig. 5), so we are confident that this is a real effect.

In Fig. 6, we show results from flash-heating the RDX-based PBX 9407. Figures 6(a) and 6(b) are IR images of the PBX pellet before and after flash-heating with 3 W of LWIR laser light at 973.3 cm^{-1}. We did not use higher laser powers even though they were available, due to safety concerns. The pellet was polished with a fine-grit polishing paper before the experiment, so the surfaces were smooth and mirror-like. The IR images in Figs. 6(a) and 6(b) show significant point-to-point variation in MWIR emissivity. These variations were a consequence of microstructure. The RDX is present in a variety of crystal habits and orientations, and RDX and binder have different MWIR emissivities.

Figure 6(c) shows the near-Gaussian LWIR laser beam profile used in the PBX measurements, obtained from a thermal image of a LWIR-irradiated glass plate. The image shows the beam intensity was nearly uniform near the beam center. Comparison of Figs. 6(a) and 6(b) show the laser created a physical and presumably a chemical change on the PBX surface. Figure 6(d) is an image obtained 450 ms after the laser was turned on, using a 100 μs integration time. Keeping in mind that our temperature determination process corrects for the emissivity on every pixel, Fig. 6(d) shows a spatially nonuniform distribution of temperature in the region where the laser beam was spatially uniform. Figure 6(e) shows an expanded view in the central region of the LWIR-heated PBX. The tiny dark spots are artifacts from bad pixels, but ignoring them, hot spots are evident, and one prominent hot spot was highlighted by a dashed circle.

F. Hot spot generation by ultrasound

Some results with several polymer-encased RDX crystals irradiated by ultrasound are shown in Fig. 7. The emissivity of the PDMS binder is less than RDX, so the MWIR image in Fig. 7(a) appeared as brighter crystals against a darker polymer background. Figures 7(b)–7(d) show a time sequence lasting 20 ms, where hot spots appeared at the locations of a few of the individual RDX crystals. Shortly after the hot spots were observed, at the same locations intense bursts of MWIR radiation were observed. From the intensities of these bursts, we infer the local temperatures were temporarily *at least as great as the ~500 K temperature* associated with rapid exothermic RDX decomposition. These rapid and highly exothermic RDX reactions appear to have occurred in time intervals less than the 10 ms spacing between adjacent frames.

In order to better understand how hot spots were generated by ultrasound in these composite solids, we performed some experiments on (nominally) nonreactive sucrose/HTPB samples with a smaller ultrasound amplitude and a more gradual heating rate than the RDX experiments. In this material, the crystals appeared darker than the polymer binder. The images in Fig. 8 make it clear that the initial deposition of heat was localized within polymer regions immediately adjacent to the sucrose crystal edges and *not* within the crystals themselves. Subsequently, the heat appearing at the polymer/crystal interfaces spread into the interior of the crystals.

IV. DISCUSSION

A. IR microscopy apparatus

The IR microscopy apparatus generated images with a resolution of 15–20 μm. We have developed a method to determine the temperature at each location within an image

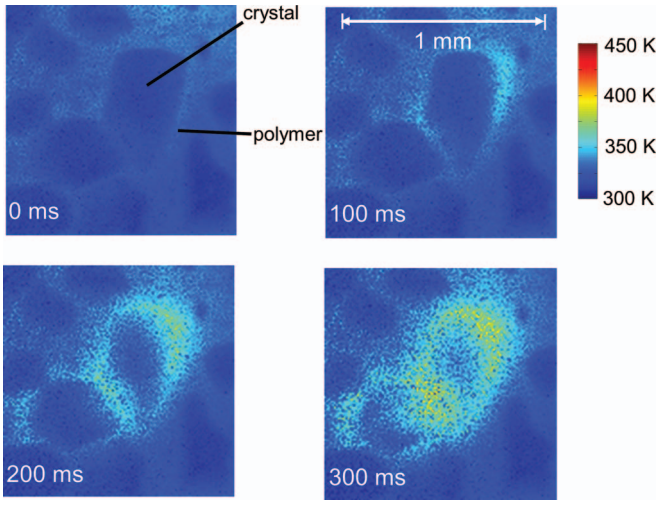

FIG. 8. IR images of a sample consisting of sucrose crystals embedded in HTPB polymer irradiated by ultrasound. These images show that ultrasound selectively inputs heat to regions of the polymer binder adjacent to crystal surfaces. The scale bar is the same for all four images.

by compensating for the temperature and wavelength dependence of the emissivity of the dielectric materials. This procedure was reliable when the emissivity could be calibrated under thermal equilibrium conditions. With thermally sensitive materials such as RDX, however, uncertainties arise. We have dealt with these uncertainties using a direct analytic continuation of the equilibrium heating data, but such extrapolations must of course introduce possible sources of error in the extended calibration. In addition, the onset of chemical reactions of the sample material may drastically change the emissivity. For instance, carbonaceous remains left behind after an EM is combusted are typically dark-colored[29] and are likely to have high emissivities. When the RDX reacts, the duration of the emission burst might be shorter than the integration time of the image capture, which would have the effect of causing an underestimation, perhaps a substantial underestimation, of the peak temperatures.

It is worth mentioning that impact-generated hot spots are usually created on the time scale of tens or hundreds of nanoseconds, since shock waves in EM propagate at speeds of a few km s^{-1}, and therefore the time needed for a shock to move across and deposit energy into a 0.1–1 mm microstructural feature would be roughly 30–300 ns.[1] The MWIR camera was specified by the manufacturer to produce single snapshots with a time gate of 0.48 μs, but in practical use 3 μs appeared to be needed to provide the full signal-capture capability. Thus, this MWIR camera could obtain an image, in single-image capture mode, as in the Woody studies,[13,14] with 3 μs time resolution, given proper synchronization and provided the hot spot was hot enough to produce significant thermal emission during that time window. We estimate, based on the results obtained here, that such high-speed single-image capture requires a minimum temperature of ~460 K.

B. LWIR generation of hot spots

Figures 5 and 6 illustrated how we could detect LWIR-generated hot spots in EM using time-resolved IR microscopy. Especially in Fig. 5, where single RDX crystals were studied, it was possible to see the creation of nascent hot spots, and the growth of the hot spots leading to sudden widespread RDX ignition.

The mechanism for hot spot generation appears to be associated with the shape (habit) and orientation of the individual crystals, and with the absorption coefficient for the LWIR light. Judging from the comparisons of the optical and IR images of the crystals in Fig. 5, hot spots were most efficiently created in regions where there was an abrupt change in the angle of the crystal surface. For instance, in two of the image streams in Fig. 5, crystals had flats that were approximately perpendicular to the LWIR beam, and the hot spots were created at the tilted surfaces adjacent to these flats. This suggests that refraction of LWIR light entering tilted crystal faces and a subsequent internal focusing may be an important factor.

It was unexpected that the LWIR light with a 25 μm penetration depth (i.e., 973.3 cm^{-1}) would create hot spots more efficiently than light with 5 μm penetration depth (i.e., 949.5 cm^{-1}). In common simplified models for laser heating,[30] the sample is a thick slab with absorption coefficient α. With heating that is adiabatic due to its short time scale, the temperature rise at the irradiated surface would be proportional to α, and the material would be uniformly heated to an approximate depth $(\alpha)^{-1}$. Thus, LWIR wavenumbers where α was larger would, in these models, be expected to produce proportionately higher uniform surface temperatures in proportionately thinner surface layers. Our observations of hot spots indicate that a portion of the incident LWIR energy has been concentrated in small volumes that have become hot enough to ignite an entire EM crystal. Broadly speaking, we can propose two possible ways that more weakly absorbing light might create more and hotter hot spots. First, there could be some kind of strongly absorbing defects scattered throughout the bulk of the crystal. The strongly absorbed LWIR might not penetrate the crystals enough to irradiate these defect sites. Second, the crystal could have some kind of static or dynamic LWIR refraction or lensing processes which would focus the incident LWIR light into spots in crystal interiors. If the LWIR light did not penetrate into the crystal, such focusing processes could not create hot spots inside the crystals.

C. Ultrasound generation of hot spots

Efforts were taken to insure that the acoustic energy was input in a spatially uniform manner. The horn was polished flat and it was contacted to smooth compliant polymer surfaces. In spite of the uniformity of the applied acoustic field, dramatic spatial nonuniformity in the resulting acoustic heating was observed, as shown in Figs. 7 and 8. Figure 7 shows that certain individual crystals were strongly heated by the ultrasound whereas others were hardly heated at all. Figure 8 shows that the initial deposition of heat occurred preferentially in regions of polymer immediately adjacent to crystal surfaces. Thus, heat deposition occurred in the more compliant polymer, as opposed to the stiffer crystals, but only at polymer/crystal interfaces where there was also a significant acoustic mismatch. We speculate it is the frictional

heating of the moving polymer surface against the more-rigid crystals that is responsible for the formation of ultrasonic hot spots in these composite materials.

V. CONCLUSIONS

We have developed a time-resolved thermal imaging microscope to study hot spots in energetic materials. The spatial resolution was on the order of 15–20 μm, and the temporal resolution was as good as 8.3 ms in image-stream mode, and could be as fast as a few μs in single-image capture mode. We also developed a method for absolute temperature measurement that overcomes the difficulties associated with the complicated wavenumber and temperature dependent emissivities of the dielectric components of the EM. Although this temperature measurement procedure is only exact when the transient images can be compared to thermal equilibrium measurements at known temperatures, by fitting our calibration data to an analytic function we could extrapolate the results to temperatures higher than those used in the calibration procedure.

In the present studies, we used two methods to input energy to the EM, a LWIR laser beam and an ultrasonic horn. In both cases, care was taken to insure that the energy input was a spatially uniform field. The MWIR thermal microscope images showed that hot spots were created with both methods of energy input, and the hot spots arose spontaneously as a consequence of sample microstructure. The hot spots proved hot enough to ignite EM such as RDX.

The mechanisms of hot spot generation were very different with LWIR and ultrasound irradiations. With LWIR, hot spots were most efficiently generated within the EM crystals themselves, and favored LWIR wavenumbers with relatively longer (25 μm) absorption depths. That finding suggests the hot spot generation mechanism involves mechanisms that concentrate LWIR energy that penetrates more deeply into the crystals. A few possibilities that need further investigation include: absorption of the LWIR light by defects in the crystal interior, focusing of the LWIR light inside the crystals by the prismatic facets, and the enhanced intensity at optical interference maxima that would not be created unless the absorption depth exceeded the 10 μm LWIR wavelength. With ultrasound, hot spots were most efficiently generated in the polymer binder immediately adjacent to the crystal surfaces. Some polymer-crystal interfaces, however, were heated to greater extent than others, which may be the consequence of variability in the polymer adhesion to individual crystal surfaces during sample preparation. In both cases, we have clearly demonstrated the utility of a fast thermal imaging microscope for the detection of hot spots in energetic materials.

ACKNOWLEDGMENTS

The research described in this study is based on work supported by the (U.S.) Office of Naval Research (ONR) under Award No. N00014-11-1-0418, the (U.S.) Air Force Office of Scientific Research (USAFOSR) under Award No. FA9550-09-1-0163, the Defense Threat Reduction Agency under Award No. HDTRA1-12-1-0011, and work supported in part by the National Science Foundation (NSF) Award No. CHE 10-11972. We thank Dr. Dan Hooks from Los Alamos National Laboratory for providing RDX samples and Professor Nick Glumac of the University of Illinois for providing PBX samples.

[1]J. E. Field, Acc. Chem. Res. **25**(11), 489 (1992).
[2]B. A. Khasainov, A. V. Attetkov, and A. A. Borisov, Chem. Phys. Rep. **15**, 987 (1996).
[3]F. P. Bowden and A. D. Yoffe, *Fast Reactions in Solids* (Academic Press, Inc., New York, 1958).
[4]M. J. Gifford, W. G. Proud, and J. E. Field, Thermochim. Acta **384**(1–2), 285 (2002).
[5]W. L. Perry, J. A. Gunderson, B. B. Glover, and D. M. Dattelbaum, J. Appl. Phys. **110**(3), 034902 (2011).
[6]A. Barua, S. Kim, Y. Horie, and M. Zhou, J. Appl. Phys. **113**(6), 064906 (2013).
[7]C. M. Tarver, S. K. Chidester, and A. L. Nichols III, J. Phys. Chem. **100**, 5794 (1996).
[8]G. Hussain and G. J. Rees, Fuel **74**(2), 273 (1995).
[9]J. E. Balzer, J. E. Field, M. J. Gifford, W. G. Proud, and S. M. Walley, Combust. Flame **130**(4), 298 (2002).
[10]W. G. Proud, AIP Conf. Proc. **620**, 1081 (2002).
[11]J. E. Balzer, C. R. Siviour, S. M. Walley, W. G. Proud, and J. E. Field, Proc. R. Soc. London, Ser. A **460**(2043), 781 (2004).
[12]W. G. Proud, I. J. Kirby, and J. E. Field, AIP Conf. Proc. **706**, 1017 (2004).
[13]D. L. Woody, J. Appl. Phys. **72**, 783 (1992).
[14]D. L. Woody, Rev. Sci. Instrum. **63**(3), 2030 (1992).
[15]P. M. Dickson, G. R. Parker, L. B. Smilowitz, J. M. Zucker, and B. W. Asay, AIP Conf. Proc. **845**(1), 1057 (2006).
[16]W. L. Perry, J. A. Gunderson, M. M. Balkey, and P. M. Dickson, J. Appl. Phys. **108**(8), 084902 (2010).
[17]K. L. McNesby and C. S. Coffey, J. Phys. Chem. B **101**, 3097 (1997).
[18]C. B. Skidmore, D. S. Phillips, S. F. Son, and B. W. Asay, AIP Conf. Proc. **429**, 579 (1998).
[19]T. G. Leighton, *The Acoustic Bubble* (Academic Press, New York, 1994).
[20]K. S. Suslick and D. J. Flannigan, Annu. Rev. Phys. Chem. **59**, 659 (2008).
[21]D. J. Flannigan and K. S. Suslick, Nature (London) **434**, 52 (2005).
[22]D. J. Flannigan and K. S. Suslick, Nat. Phys. **6**, 598 (2010).
[23]Y. Didenko and K. S. Suslick, Nature (London) **418**, 394 (2002).
[24]H. Kim, A. Lagutchev, and D. D. Dlott, Propell. Explos. Pyrotech. **31**, 116 (2006).
[25]S. A. Sheffield, R. L. Gustavsen, and R. R. Alcon, AIP Conf. Proc. **429**(1), 575 (1998).
[26]R. Infante-Castillo, L. Pacheco-Londoño, and S. P. Hernández-Rivera, Spectrochim. Acta A **76**(2), 137 (2010).
[27]G. Barton, *Elements of Green's Functions and Propagation: Potentials, Diffusion and Waves* (Oxford University Press, Oxford, 1989).
[28]M. Vollmer and K. P. Möllmann, *Infrared Thermal Imaging: Fundamentals, Research and Applications* (Wiley-VCH, Hoboken, NJ, 2010).
[29]R. Behrens, J. Phys. Chem. **94**, 6706 (1990).
[30]E. Matthias, M. Reichling, J. Siegel, O. W. Käding, S. Petzoldt, H. Skurk, P. Bizenberger, and E. Neske, Appl. Phys. A **58**(2), 129 (1994).